Optics Letters

Vertical mode transition in hybrid lithium niobate and silicon nitride-based photonic integrated circuit structures

Abu Naim R. Ahmed,[1,*] Andrew Mercante,[1] Shouyuan Shi,[1] Peng Yao,[2] and Dennis W. Prather[1]

[1]School of Electrical and Computer Engineering, University of Delaware, Newark, Delaware 19716, USA
[2]Phase Sensitive Innovations, Newark, Delaware 19711, USA
*Corresponding author: naimece@udel.edu

Received 17 July 2018; revised 25 July 2018; accepted 27 July 2018; posted 31 July 2018 (Doc. ID 339986); published 22 August 2018

This Letter presents an optical mode transition structure for use in $Si_3N_4/LiNbO_3$-based hybrid photonics. A gradual modal transition from a Si_3N_4 waveguide to a hybrid $Si_3N_4/LiNbO_3$ waveguide is achieved by etching a terrace structure into the sub-micrometer thick $LiNbO_3$ film. The etched film is then bonded to predefined low pressure chemical vapor deposition Si_3N_4 waveguides. Herein we analyze hybrid optical devices both with and without the aforementioned mode transition terrace structure. Experimental and simulated results indicate that inclusion of the terrace significantly improves mode transition compared to an abrupt transition, i.e., a 1.78 dB lower mode transition loss compared to the abrupt transition. The proposed transition structure is also applied to the design of hybrid Si_3N_4-$LiNbO_3$ micro-ring resonators. A high-quality factor (Q) resonator is demonstrated with the terrace transition which mitigates undesired resonances.

OCIS codes: (040.6040) Silicon; (130.3730) Lithium niobate; (230.0230) Optical devices; (130.0130) Integrated optics; (250.5300) Photonic integrated circuits.

https://doi.org/10.1364/OL.43.004140

The integration of electro-optic (EO) $LiNbO_3$ with passive Si photonics has attracted significant interest in the optical communication community [1–10]. Hybrid devices have the potential to realize many photonic devices by means of combining the desirable properties of dissimilar materials: tunable micro-ring resonators [3,5,6], Mid-IR modulators [7], Mach–Zehnder modulators [1], and wavelength converters [10]. The heterogeneous integration of $LiNbO_3$ with Si on insulator (SOI) is currently at the forefront of hybrid $LiNbO_3$ device research [1,3,5–7,9,10]. This is likely due to the low material cost of Si, established SOI fabrication technology, and the high index contrast between Si and $LiNbO_3$, which facilitates low complexity optical mode transition designs [9]. An equivalently simple solution for fabricating $Si_3N_4/LiNbO_3$ hybrid EO devices has yet to be implemented despite the ultra-low propagation loss [11–13], high power handling capabilities [14], and wide transparent spectrum [13] that high-quality low pressure chemical vapor deposition (LPCVD) Si_3N_4 possesses. One of the major challenges of designing this $Si_3N_4/LiNbO_3$ hybrid device is in achieving a low loss optical mode transition from the Si_3N_4 waveguide to hybrid $Si_3N_4/LiNbO_3$ [2]. Bonding $LiNbO_3$ directly on the top of the predefined Si_3N_4 waveguide imposes a significant mode transition loss at the interface due to reflections caused by a substantial disparity in effective indices and mode profiles between Si_3N_4 and hybrid $Si_3N_4/LiNbO_3$ guided optical modes. A tapered Si_3N_4 mode transition has been implemented with success [8], but the device fabrication is complex and requires precise alignment during bonding.

In this work, we present a simplified but efficient mode converter structure to obtain a low transition loss from the Si_3N_4 waveguide to the hybrid $Si_3N_4/LiNbO_3$ structure. With the application of the mode transition structure, a hybrid $Si_3N_4/LiNbO_3$ single bus micro-ring resonator has been demonstrated. Our process uses commercial-off-the-shelf (COTS) LPCVD Si_3N_4 on quartz, and thin film $LiNbO_3$ on insulator (LNOI) wafers. The general process flow is as follows: fabricate passive Si_3N_4 waveguides, etch terrace structures into the $LiNbO_3$, and then bond the two structures together. Some advantages of our approach are that it facilitates a low-loss transition, allows for relaxed alignment requirements during the bonding process, and conserves the high-cost thin film $LiNbO_3$ wafer by selectively bonding only in the desired location of the photonic circuit. This paper is organized by first presenting a simulation of the hybrid waveguide and mode transition structure, then discussing the device fabrication and characterization.

The passive hybrid photonic device proposed in this Letter consists of three types of optical waveguide structures: standalone Si_3N_4 ridge waveguides for optical input and output, a hybrid ($Si_3N_4/LiNbO_3$) EO waveguiding region suitable for hosting active devices, and a mode transition structure residing between the standalone Si_3N_4 and hybrid waveguide sections, shown in Fig. 1.

We first conduct a parametric study to investigate the impact of the Si_3N_4 ridge thickness and width, as well as $LiNbO_3$'s thickness on mode confinement in the $LiNbO_3$ and device bending radius. Our primary interest is finding

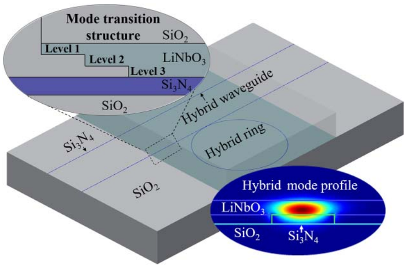

Fig. 1. Schematic of the proposed structure. The top left is the side-view of the mode transition structure, and the bottom right is the intensity mode profile of the hybrid $Si_3N_4/LiNbO_3$ waveguide.

an optimal device structure that maximizes the mode confinement in the $LiNbO_3$ and does not introduce excessive bending loss in the hybrid waveguide. The device is designed to support a single TE-polarized fundamental mode at a wavelength of 1550 nm. The proposed device is simulated using commercial Lumerical Mode solver software. The design parameters include Si_3N_4 core width of W_{Si3N4}, core thickness of T_{Si3N4}, and the *x*-cut $LiNbO_3$ film thickness of T_{LN}. Figure 2(a) shows the simulated confinement factor map, which visualizes the optical mode confinement factor in $LiNbO_3$ (Γ_{LN}) as function of W_{Si3N4} and T_{LN} for 200 nm T_{Si3N4}. We define Γ_{LN} as the ratio of the power residing in the $LiNbO_3$ compared to the total power present in the hybrid guided mode. The confinement factor falls by ∼10% as W_{Si3N4} rises from 0.5 to 2 μm because of increased mode confinement in the Si_3N_4 core, while Γ_{LN} increases by 20% from 300 to 800 nm $LiNbO_3$ thickness as it pulls the light from Si_3N_4 due to its higher index. However, the bending radius significantly increases for the thicker $LiNbO_3$, as shown in Fig. 2(b), due to the lack of optical mode confinement in the Si_3N_4 core region. Furthermore, a thinner $LiNbO_3$ film will help to reduce mode transition loss from standalone Si_3N_4 to the hybrid device. A thinner and narrower loading Si_3N_4 strip provides a higher optical confinement factor, however, it results in lower index contrast in the horizontal direction, leading to increased bending loss. By considering the above tradeoff study, a hybrid waveguide with a cross section of a 1.7 μm wide and 200 nm thick Si_3N_4 strip loaded to a 300 nm thick $LiNbO_3$ is chosen, which can support a more compact bending radius of ∼250 μm, higher mode confinement in $LiNbO_3$ of 0.63, and lower mode transition loss.

As the thin film $LiNbO_3$ is locally bonded to the Si_3N_4 waveguide, an efficient mode transition from the Si_3N_4 waveguide to the hybrid waveguide is required. To this end, a mode converter structure is designed to achieve a low transition loss from the Si_3N_4 waveguide to the hybrid $Si_3N_4/LiNbO_3$ waveguide region. For low loss transition, we etch the edge of the $LiNbO_3$ film in two steps to form a terrace shape as shown in Fig. 1, top inset. The terrace $LiNbO_3$ film is bonded on the top of the Si_3N_4 waveguide. The terrace structure has only a step shape in the optical mode propagation direction and is uniform in the other direction. Such a feature eliminates any critical alignment requirement during the bonding process. For reference, a $LiNbO_3$ sample without a terrace transition structure is also investigated. Full 3D EM simulation of the coupling devices are simulated using Lumerical 3D FDTD simulation software. Figure 3 shows the intensity profile of the mode transition from the Si_3N_4 to the hybrid waveguides. In the non-etched rectangular $LiNbO_3$, due to the discontinuity of the high index of $LiNbO_3$ substrate, large scattering or reflection from the coupling is observed. The simulated mode transition loss per interface is 2.67 dB for non-etched $LiNbO_3$, shown in Fig. 3(a). By introducing our proposed two-step transition this transition loss can be reduced to 0.81 dB. The gradual mode transition at three different locations in the terrace structure indicated as (i), (ii), and (iii) in Fig. 3(b) are shown in Figs. 3(c)–3(e). As the $LiNbO_3$ thickness increases, more light is confined in the $LiNbO_3$ cladding region. The height of each step is 100 nm,

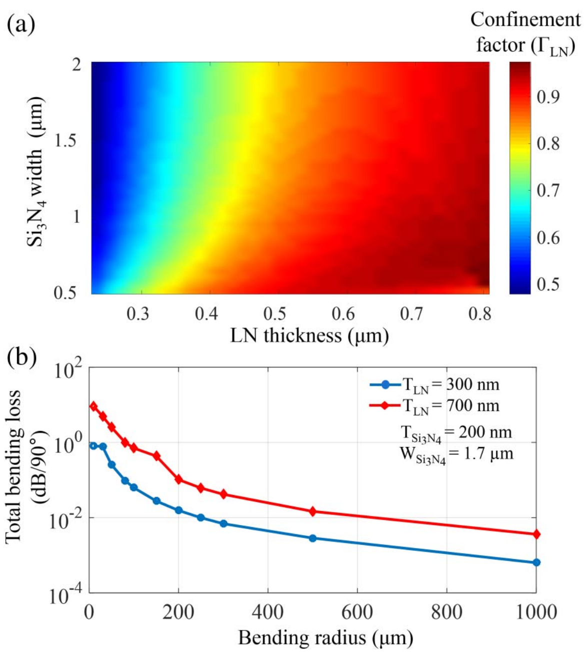

Fig. 2. (a) Simulated mode confinement factor in $LiNbO_3$ (Γ_{LN}) as a function of Si_3N_4 strip width and $LiNbO_3$ film thickness at 1550 nm for the fundamental TE mode. (b) The simulated bending loss of the hybrid waveguide as a function of bending radius for 300 nm and 700 nm $LiNbO_3$ film thickness.

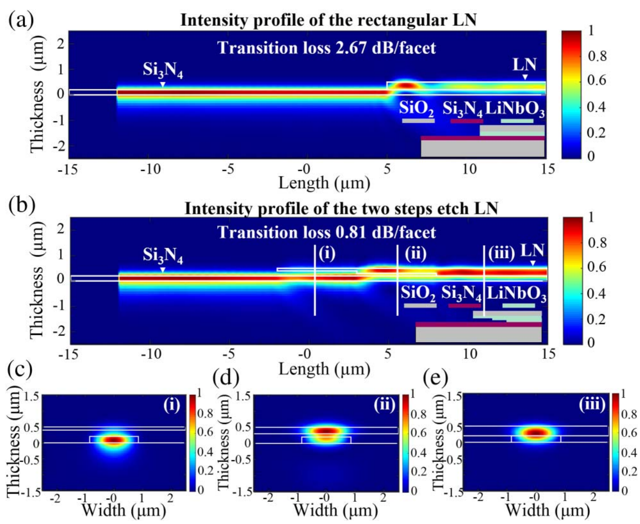

Fig. 3. Intensity profiles showing the mode transition from Si_3N_4 to the hybrid $Si_3N_4/LiNbO_3$ waveguides in the cases of (a) 300 nm rectangular $LiNbO_3$, (b) two steps etched in $LiNbO_3$ mode transition structure. The right-sided images (c)–(e) show the mode intensity evolution along the transition structure of (b) at three different positions.

and regions (i) and (ii) are each 5 μm in length, making the total length of the transition region 10 μm.

A schematic of the fabrication process is shown in Fig. 4. Silicon nitride waveguide fabrication begins with a commercial LPCVD Si_3N_4 on a quartz wafer (Mark Optics). The 200 nm thick LPCVD layer offers a homogeneous refractive index, uniform thickness, chemical stability, and low optical absorption at our operational wavelength. A 90 nm thick Cr layer is deposited on the insulating substrate to mitigate the charging phenomenon during e-beam lithography. Device features are defined in an AR-N 7520 negative tone resist using e-beam lithography.

The resist patterns are transferred into the underlying Cr using Cl_2 (45 sccm)/O_2 (2 sccm) inductively coupled plasma (ICP) reactive-ion etching. Afterward, the device pattern is transferred into the Si_3N_4 layers using a SF_6 (5 sccm)/C_4F_8 (5 sccm)/Ar (90 sccm) etch. Then, the excess photoresist, Cr, and other etching byproducts are removed using O_2 plasma clean and wet chemical cleaning processes. Fabricated Si_3N_4 structures are shown in Fig. 5(a); their measured dimensions for height and width are 200 nm and 1.7 μm, respectively. Along with straight waveguides, micro-ring resonators are fabricated on Si_3N_4. Figure 5(a) shows the top-down view of the fabricated micro-ring and its coupling region. A thin film $LiNbO_3$ is etched to produce the simulated mode transition structure. The *x*-cut LNOI wafers are purchased from NANOLN; the wafers consist of a 300 nm-thick $LiNbO_3$ device layer affixed to a 500 μm-thick fused silica handle. A 120 nm chromium layer is sputtered on the thin film $LiNbO_3$ as a hard mask, then the positive resist is spin-coated and patterned by UV-lithography to define the first level of the mode transition structure. The pattern is then transferred to the substrate using Cr dry etching, as mentioned above, followed by time multiplexed $LiNbO_3$ etching by CF_4 (6 sccm)/N_2 (28 sccm)/O_2 (0.5 sccm) plasma dry etch. The etch rate of *x*-cut $LiNbO_3$ is ~32 nm/ min in a 600 W plasma under 400 W bias, and the surface roughness is ±8 nm. The remaining photoresist and Cr mask layer are removed by the wet etching solution. The second etch height is fabricated in the same fashion. Figure 5(b) shows the SEM image of the final mode transition structure after the two steps have been defined. The levels described in the Fig. 5(b) are comparable to the levels defined in Fig. 1. Level 1 is the thinnest part of the transition region which is 100 nm thick, level 2 is the 200 nm thick middle section, and level 3 is the 300 nm thick section which is the bonding surface of the $LiNbO_3$. Next, we bond the Si_3N_4 and $LiNbO_3$ samples together indirectly with Benzocyclobutene (BCB) [15] procured from DOW. A ~250 nm thick BCB layer is spun over the top of the Si_3N_4 device layer, and the BCB is diluted with mesitylene to reduce spin on thickness. The BCB coated wafer is then soft baked for 1 min at 150°C, to let the excess solvent evaporate. The BCB coated Si_3N_4 substrate is placed into a nitrogen purged vacuum oven for precuring at ~180°C for 5 min, resulting in a BCB thickness of ~230 nm, leaving a ~30 nm bonding layer between the $LiNbO_3$ and Si_3N_4 devices. The thin film's $LiNbO_3$ substrate is bonded face down on top of the target Si_3N_4 wafer using the flip-chip bonder. A bonding weight of 9,000 g is applied through the bond-head. The sample is under load for 150 s at 150°C. The bonded wafer stack is placed back into a nitrogen purged vacuum oven set at 200°C for 15 h to complete the polymerization of the BCB. Finally, the waveguide end-facet is prepared by a dicing and polishing technique for efficient fiber coupling. Figures 5(c) and 5(d) show the microscopic images of the bonded devices.

The hybrid waveguides are characterized using a tunable semiconductor laser near 1550 nm. Transverse electric polarized light is edge coupled into and out of the Si_3N_4 waveguide via polarization maintaining lensed fibers. Exiting light is directed into a photodetector then a transimpedance amplifier. The optical intensity as a function of wavelength can then be observed on an oscilloscope. Figure 6 shows the measured insertion loss spectra for three 1.3 cm long devices: a standalone Si_3N_4 reference waveguide, a hybrid waveguide with a mode transition structure, and a hybrid waveguide without transition structure. The hybrid waveguides consist of 0.4 cm long input and output Si_3N_4 waveguides with a 0.5 cm long hybrid region residing in between. The hybrid transition loss can be obtained by comparing the measured insertion loss spectra of the three different waveguides.

At 1550 nm, the measured mode transition loss difference per interface between the two hybrid waveguides is 1.78 dB, which is comparable to our simulation result. This implies the mode transition loss of ~0.81 dB per interface for the terrace transition structure. The total insertion loss can be further

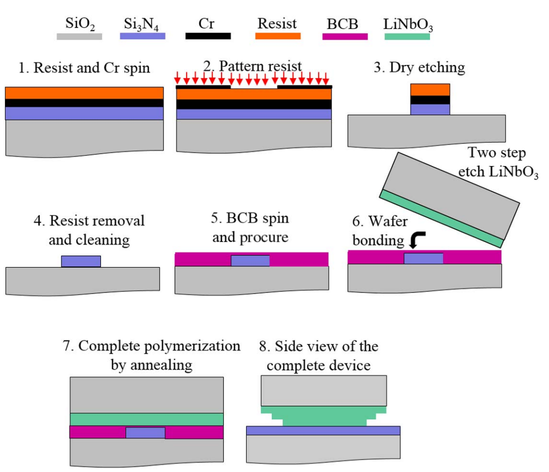

Fig. 4. Fabrication process of the complete hybrid device. Step 1 to step 7 are the device cross-section, and step 8 is the side view of the device.

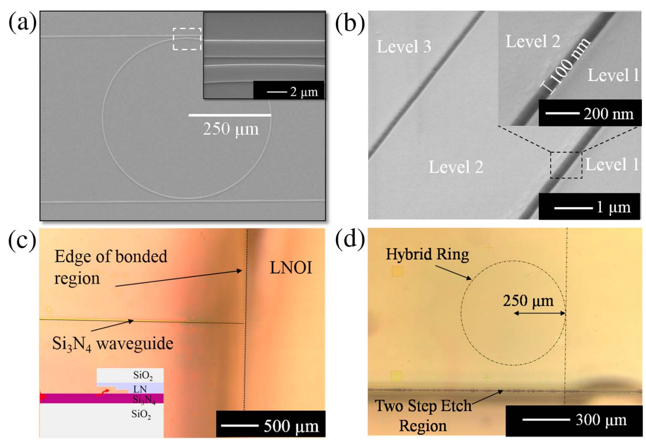

Fig. 5. (a) SEM images in a top-down view of a fabricated ring on Si_3N_4, inset shows the smooth sidewall ring coupling region, (b) top view of the two steps etch $LiNbO_3$ by ICP-RIE, and inset shows the level 1 sidewall, (c) microscopic image of the straight waveguide region after flip-chip bonding, (d) microscopic image of the hybrid ring.

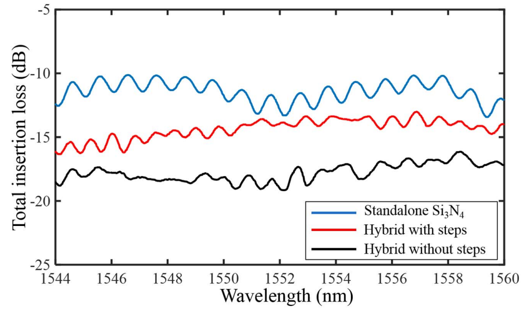

Fig. 6. Total insertion loss spectrum as a function of wavelength for a standalone Si_3N_4 ridge, a hybrid structure with the step transition, and the hybrid structure without any fabricated transition.

reduced by introducing a top cladding layer at the input/output Si_3N_4 waveguides and thinning the Si_3N_4 core dimension [12,16]. This, however, leads to the larger footprint of the photonic devices [12]. A single micro-ring of 250 μm radius with a single bus waveguide is fabricated and characterized with and without the mode transition terrace structure. The measured transmission spectrum for TE polarization is scanned using a Keysight tunable laser near 1550 nm. The hybrid ring without the terrace mode transition structure has illustrated multiple free spectral ranges (FSRs). In Fig. 7, three FSRs are clearly distinguishable. The measured FSR 2 (0.87 nm) is close to the theoretical FSR value of the ring (0.79 nm). The FSR 1 and FSR 3 are observed due to the presence of multiple cavities and reflections of the non-smooth transition region from Si_3N_4 to the hybrid $Si_3N_4/LiNbO_3$ waveguide. The transmission spectrum of the hybrid micro-ring with the terrace transition is plotted in Fig. 8(a). The spectrum shows only one clear FSR over the interested wavelength range, which indicates that the terrace structure significantly improves the transition and mitigates multiple cavities and reflections. The obtained transmission spectrum is fitted to a Lorentzian curve, Fig. 8(b), to extract the key resonator characteristics [17]. The free spectral range ($\Delta\lambda_{FSR}$) of the resonator is about 0.76 nm. The calculated finesse, F, the intrinsic quality factor, (Q), and the loss coefficient are 13, $\sim 6 \times 10^4$, and 0.6 cm^{-1}, respectively, at a resonant wavelength of 1551.39 nm. The group index (n_g) of the waveguide can be calculated from the measured FSR of the hybrid ring. The calculated group index value is within the 4% range of the simulated group index, which illustrates that the $LiNbO_3$ film is optically bonded to the Si_3N_4.

In summary, a hybrid $Si_3N_4/LiNbO_3$ material system along with novel mode transition structure is designed, fabricated,

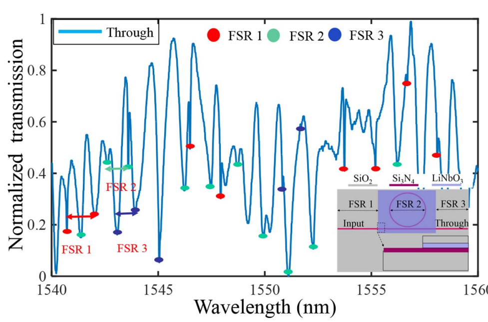

Fig. 7. Transmission spectrum at the through port of the hybrid micro-ring resonator without the terrace transition shows multiple FSRs.

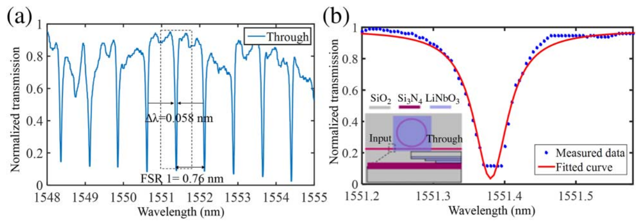

Fig. 8. (a) Transmission spectrum at the through port of the hybrid micro-ring resonator with mode transition structure shows one clear FSR; (b) Lorentzian fit of the highlighted peak.

and characterized. The proposed device is optimized for minimum bending radius, high mode confinement in the $LiNbO_3$ region, and low mode transition loss. A 10 μm long and two steps etch terrace transition structure in the thin film $LiNbO_3$ exhibits a mode transition loss of ∼0.81 dB from Si_3N_4 to the hybrid $Si_3N_4/LiNbO_3$ waveguide. This improved the mode transition loss by 1.78 dB in comparison to when steps are absent. Hybrid micro-ring resonators with and without mode transition are compared, and a clean spectrum of single FSR and a smooth mode transition are demonstrated by introducing the mode transition structure.

Funding. Air Force Office of Scientific Research (AFOSR) (FA9550-17-1-0071).

REFERENCES

1. P. O. Weigel, M. Savanier, C. T. DeRose, A. T. Pomerene, A. L. Starbuck, A. L. Lentine, V. Stenger, and S. Mookherjea, Sci. Rep. **6**, 22301 (2016).
2. A. Boes, B. Corcoran, L. Chang, J. Bowers, and A. Mitchell, Laser Photon. Rev. **12**, 1700256 (2018).
3. L. Chen, Q. Xu, M. G. Wood, and R. M. Reano, Optica **1**, 112 (2014).
4. P. Rabiei, J. Ma, S. Khan, J. Chiles, and S. Fathpour, Opt. Express **21**, 25573 (2013).
5. L. Chen, M. G. Wood, and R. M. Reano, Opt. Express **21**, 27003 (2013).
6. L. Chen and R. M. Reano, Opt. Express **20**, 4032 (2012).
7. J. Chiles and S. Fathpour, Optica **1**, 350 (2014).
8. L. Chang, M. H. Pfeiffer, N. Volet, M. Zervas, J. D. Peters, C. L. Manganelli, E. J. Stanton, Y. Li, T. J. Kippenberg, and J. E. Bowers, Opt. Lett. **42**, 803 (2017).
9. J. D. Witmer, J. T. Hill, and A. H. Safavi-Naeini, Opt. Express **24**, 5876 (2016).
10. L. Chang, Y. Li, N. Volet, L. Wang, J. Peters, and J. E. Bowers, Optica **3**, 531 (2016).
11. J. F. Bauters, M. J. Heck, D. John, D. Dai, M.-C. Tien, J. S. Barton, A. Leinse, R. G. Heideman, D. J. Blumenthal, and J. E. Bowers, Opt. Express **19**, 3163 (2011).
12. T. A. Huffman, G. M. Brodnik, C. Pinho, S. C. Gundavarapu, D. Baney, and D. J. Blumenthal, IEEE J. Sel. Top. Quantum Electron. **24**, 5900209 (2018).
13. R. Baets, A. Z. Subramanian, S. Clemmen, B. Kuyken, P. Bienstman, N. Le Thomas, G. Roelkens, D. Van Thourhout, P. Helin, and S. Severi, *Optical Fiber Communications Conference and Exhibition (OFC)* (2016).
14. M.-C. Tien, J. F. Bauters, M. J. Heck, D. J. Blumenthal, and J. E. Bowers, Opt. Express **18**, 23562 (2010).
15. D. Liang, G. Roelkens, R. Baets, and J. E. Bowers, Materials **3**, 1782 (2010).
16. N. Daldosso, M. Melchiorri, F. Riboli, M. Girardini, G. Pucker, M. Crivellari, P. Bellutti, A. Lui, and L. Pavesi, J. Lightwave Technol. **22**, 1734 (2004).
17. W. Bogaerts, P. De Heyn, T. Van Vaerenbergh, K. De Vos, S. Kumar Selvaraja, T. Claes, P. Dumon, P. Bienstman, D. Van Thourhout, and R. Baets, Laser Photon. Rev. **6**, 47 (2012).